Vol. 21, No. 1(2022) Cat2434
Revista Mexicana de Ingeniería Química

Design equations based on micro/macromixing theoretical analysis of RTD curves for a tubular concentric electrochemical reactor with expanded meshes as electrodes

Ecuaciones de diseño de un reactor electroquímico tubular con electrodos concéntricos de mallas expandidas a través de un análisis teórico del micro/macromezclado de curvas de DTR

M.I. Jaramillo-Gutiérrez[1], J.A. Pedraza-Avella[1], I. González[2], E.P. Rivero[3], M.R. Cruz-Díaz[3]*

[1] *Grupo de Investigaciones en Minerales, Biohidrometalurgia y Ambiente - GIMBA, Universidad Industrial de Santander - UIS, Sede Guatiguará, Transv. Guatiguará, Calle 8N No. 3W-60, Barrio El Refugio, C.P. 681011, Piedecuesta (Santander), Colombia.*

[2] *Departamento de Química, Universidad Autónoma Metropolitana-Iztapalapa. San Rafael Atlixco 186, C.P.09340, Ciudad de México, México.*

[3] *Universidad Nacional Autónoma de México - UNAM, Facultad de Estudios Superiores Cuautitlán, Campo 1, Departamento de Ingeniería y Tecnología, Av. 1° de Mayo S/N, Col. Sta. María las Torres, C.P. 54740, Cuautitlán Izcalli (Edo. Méx.), México*

Received: April 18, 2021; Accepted: December 7, 2021

Abstract

In the present work, the liquid flow pattern in a Tubular Electrochemical Reactor (T-ECR) with concentric cylindrical expanded meshes as electrodes and inlet/outlet distributors of shower sprinkler type was evaluated. It was found that the CFD theoretical results describe the experimental $F(t)$-curves obtained with the methodology of "step-signal input". Later, the $F(t)$-curves estimated with CFD for each reactor zone were adequately approximated with global parametric models for the development of the T-ECR design equations. The Stagnant Zone Model with mass exchange with the anodic zone turns out to be adequate for the reactor shell zone. However, for the cathode and anode meshes, the Axial Dispersion Model with mass exchange between them proves to be appropriate. For all liquid flow rates (0.37 to 4.0 L min^{-1}), the dispersion numbers (N_d) are in a magnitude order of small dispersion ($D_{ax}/u_{int}L_z \approx 0.01$). This confirms that the incorporation of inlet/outlet distributors in a T-ECR improve considerably the liquid flow pattern behaviour. This experimental methodology, coupled with micro/macromixing theoretical analysis of RTD curves with CFD, can be a good alternative for the reactor design.

Keywords: Tubular Electrochemical Reactor, Cylindrical expanded meshes as electrodes, RTD by Computational Fluid Dynamic, RTD by the step-signal, Micromixing and Macromixing analysis.

Resumen

En el presente trabajo se evaluó el patrón de flujo de líquido en un Reactor Electroquímico Tubular (RET) con electrodos de mallas expandidas concéntricas y distribuidores de entrada/salida de tipo regadera. Se encontró que los resultados teóricos de CFD describen las funciones acumulativas (curvas $F(t)$) obtenidas con la técnica de "señal de entrada escalón". Posteriormente, utilizando CFD se estimaron las curvas $F(t)$ para cada zona del reactor, las cuales se aproximaron con modelos paramétricos globales para plantear las ecuaciones de diseño del RET. En la zona entre la carcasa del reactor y la malla anódica el Modelo de Zona Estancada con intercambio de masa resulto adecuado. Sin embargo, en las mallas catódica y anódica, el Modelo de Dispersión Axial con intercambio de masa entre las mallas es apropiado. Para todos los caudales de líquido (0.37 a 4.0 L min^{-1}), los números de dispersión (N_d) están en un orden de magnitud de baja dispersión ($D_{ax}/u_{int}L_z \approx 0.01$). Esto confirma que la incorporación de distribuidores de entrada/salida en un RET mejora considerablemente el comportamiento del patrón de flujo de líquido. La metodología experimental, junto con el análisis teórico de micro/macromezclado de curvas RTD con CFD, puede ser una buena alternativa para el diseño del reactor.

Palabras clave: Reactor Electroquímico Tubular, Electrodos de mallas expandidas cilíndricas, Distribución de tiempos de residencia (DTR), Trazador en señal escalón, Análisis de micro/macromixing.

* *Corresponding author. E-mail*: cdmrmartin@hotmail.com
https://doi.org/10.24275/rmiq/Cat2434
ISSN:1665-2738, *issn-e*: 2395-8472

1 Introduction

Recently, different configurations have been proposed for tubular electrochemical (T-ECR) and photoelectrochemical (T-PECR) reactors with cylindrical expanded meshes (CEMs), as electrodes, used for wastewater treatment. In annular PECR, an UV lamp encased in a quartz tube is installed in the center of the reactor, while in the annular space cylindrical expanded meshes are placed. This configuration has been used for degradation or oxidation of different pollutants. For instance, disinfection of *E. coli* and 4-nitrophenol (Christensen *et al*., 2003; 2005); treatment of landfill leachate (Zhao *et al*., 2010); discoloration of azo dyes from synthetic or real textile wastewater (Moraes *et al*., 2007; Turolla *et al*., 2012; 2018; Cardoso *et al*., 2016); methanol oxidation (Marugán *et al*., 2013; Pablos *et al*., 2014); destruction of Cu-EDTA complex and recovery of liberated Cu2+ ions (Zhao *et al*., 2014).

In the case of T-ECR or T-PECR, the electrodes of CEM are installed in concentric tubular arrangement, under this configuration different processes have been carried out, e.g., elimination of Cr(VI) on spiral anode (Martínez-Delgadillo *et al*., 2010); copper removal by cementation process (Djoudi *et al*., 2012); red methyl degradation (Ibrahim *et al*., 2013); phenol degradation (Wang *et al*., 2015); diuron degradation (Barbosa de Matos *et al*., 2020); electrochemically assisted photocatalytic (EAP) disinfection of rainwater under real sun conditions (McMichael *et al*., 2021).

Commonly, the inlet/outlet distributors are a critical factor in reactor performance, since its function is to generate a flow pattern that promotes an efficient and homogenous mass transport towards the reaction site. In the above-mentioned works, usually the feed and output of the liquid phase are done through tubes (centered, lateral, or tangential), under this inlet/outlet liquid configuration, CFD studies have shown that the tubular geometry reactors exhibit a non-homogeneous flow and dead volumes at the entrance and exit; high and low velocity peaks were also observed along the reactor. In addition, considerable distances are required to achieve a fully developed flow; while at low liquid flows a non fully developed velocity profiles were observed (Martínez-Delgadillo *et al*., 2010; Su *et al*., 2011; Djoudi *et al*., 2012; Ibrahim *et al*., 2013; Wang *et al*., 2015; Casado *et al*., 2017; Ariza *et al*., 2018; Barbosa de Matos *et al*., 2020; Jaramillo-Gutiérrez *et al*., 2020).

Particularly, the RTD technique has been used to evaluate the behaviour of the liquid flow pattern within a reactor, also to validate the theoretical results of CFD, different experimental methods have been implemented, some of them provide a global description of the liquid flow pattern (macromixing), such as fluid visualisation within the flow channel by dye injection (Casado *et al*., 2017; Ariza *et al*., 2018; Djoudia *et al*., 2012; Barbosa de Matos *et al*., 2020; Jaramillo-Gutiérrrez *et al*., 2020). Other techniques as the particle tracking methods, e.g., laser-induced fluorescence (Fitch and Ni, 2003), radiotracers (Upadhyay *et al*., 2013; Roy S., 2017) and ultrasonic doppler velocimetry (Takeda, 1999; Jaramillo-Gutiérrrez *et al*., 2020), can describe the local velocity of the liquid flow pattern (micromixing) in different directions and reactor zones.

The application of these experimental methods for describing the RTD or velocity field in T-ECR or T-PECR with CEMs, present two drawbacks; with the stimulus-response technique is not possible to obtain RTD curves for each reactor zones (inside the internal cylinder, and in the annular spaces between the electrodes and the reactor shell), while with a particle tracking method is difficult obtain RTD curves in each internal zone because the CEMs distort the signal received by the detector, causing poor data interpretation.

To overcome these difficulties, tracer experimental methods should be complemented with mathematical modelling and CFD studies; e.g., (a) parametric mathematical models of RTD (at a macromixing scale), such as N-tanks in series model (N-TIS), axial dispersion model (ADM) and plug dispersion exchange model (PDEM) or combination between them (Djoudi *et al*., 2012; Ariza *et al*., 2018; Barbosa de Matos *et al*., 2020; Jaramillo-Gutiérrrez *et al*., 2020) or (b) numerical simulation of RTD by CFD, using the Navier-Stokes equations and the diffusion-convection equation (laminar or turbulent regime) for describing the liquid flow pattern at a micromixing scale (Martínez-Delgadillo *et al*., 2010; Su *et al*., 2011; Ibrahim *et al*., 2013; Casado *et al*., 2017; Ariza *et al*., 2018; Jaramillo-Gutiérrrez *et al*., 2020).

In the case of RTD predictions with turbulent models (standard $k-\varepsilon$, RNG $k-\varepsilon$, and Reynolds stress model, etc.), can lead to dissimilarities with those obtained by the experimental pulse signal technique (Cruz-Díaz *et al*., 2014). To overcome this problem, it is preferable to use a tracer stimulus of step signal input because this experimental technique does not depend on the intensity of the injection pulse, nor

on the mathematical function of the injection pulse introduced to computational simulation (Casado *et al*., 2017; Ariza *et al*., 2018; Jaramillo-Gutiérrrez *et al*., 2020). Therefore, to ensure an acceptable approximation of the RTD by CFD, comparison with experimental RTD is essential before applying CFD in practice to predict the flow behaviour of the industrial systems.

The aim of this work is to evaluate the liquid flow pattern of a tubular reactor with CEMs (T-ECR or T-PECR) and inlet/outlet distributors of shower sprinkler type. The experimental methodology of step signal input will be implemented to validate the cumulative function ($F(t)$-curves) obtained with CFD (COMSOL Multiphysics 5.3). Subsequently, using CFD will be estimated the RTD curves in different zones of the tubular reactor (within inner cylinder and in the annular spaces between the electrodes and the reactor shell). This estimation will be approximated with global parametric models (ADM or PDEM) to obtain the design equations of the T-PECR and the characteristic parameters (axial dispersion coefficient, mass transfer units, and liquid hold-up ratio).

2 Experimental

2.1 Experimental set-up

The experimental study was performed in a bench-scale tubular reactor with CEMs (see Fig. (1a)) composed of three main parts: (1) the inlet distributor, (2) reaction zone, and (3) outlet distributor. The reaction zone contains two electrodes (see Fig. (1b)): a (photo)anode forming the outer cylinder, and the cathode forming the inner one. The (photo)anode is a grade 2 titanium expanded mesh (Stanford advanced material PT22 TM), coated with sol gel TiO2 film. The cathode is an AISI/SAE 304 stainless steel expanded mesh (Colmallas IMT-10 Cold Rolled), nickel-plated (Ni/SS) by electrodeposition. The procedure of preparation of both electrodes were previously reported by Jaramillo-Gutiérrez *et al*. (2016). The dimensions of tubular reactor with CEMs are reported in Table 1.

An important aspect to be highlighted in Fig. 1(a) is the presence of a vertical cylindrical duct in the outlet manifold (right upper part). It will be used not only for the exit of the gases generated during the electrolysis (i.e., hydrogen production) but also as a space to introduce the electrical conductor to energize the reactor. For this reason, no liquid exit holes are located in this area.

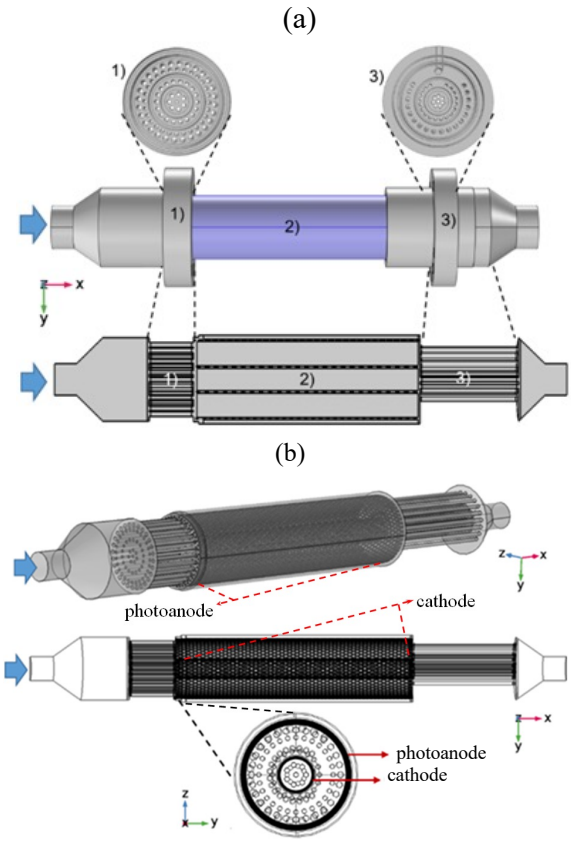

Fig. 1 (a) Tubular (photo)electrochemical reactor with concentric cylindrical expanded meshes as electrodes (upper figure): 1) inlet distributor, 2) (photo)electrocatalytic reaction zone, and 3) outlet distributor with vertical duct for current supply. Lower figure: longitudinal view which shows the internal parts of the T-PECR. (b) The internal structure of the tubular reactor with CEMs: a photoanode forming the cylindrical outer electrode, and the cathode forming the cylindrical inner electrode.

Table 1. Dimensions of tubular reactor with CEMs.

Description	Dimensions and unit
Reaction zone volume	0.0011 (m^3)
Reaction zone diameter	0.075 (m)
Total length	0.500 (m)
Tube outside diameter	0.092 (m)
Photoanode and cathode length	0.250 (m)
Photoanode inside diameter	0.061 (m)
Photoanode outside diameter	0.067 (m)
Cathode inside diameter	0.018 (m)
Cathode outside diameter	0.024 (m)

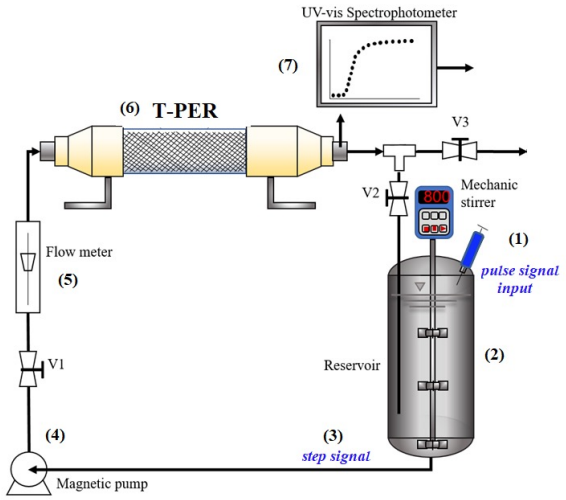

Fig. 2 Photoelectrochemical reactor schema and its liquid flow system for the RTD experiments. (1) pulse signal injection point, (2) continuous stirring tank, (3) step signal that enters to T-PER, (4) centrifugal pump (5) flow meter, (6) tubular photoelectrochemical reactor (T-PER), (7) UV-vis spectrophotometer in-line. Valve V1 regulates volumetric flow, valve V2 stops recirculation of liquid flow, and V3 discharges liquid flow to drain.

A schematic diagram of the tubular reactor with CEMs and the pipeline of the recirculation system used in the RTD experimental study are shown in Fig. 2.

The liquid phase was contained in a 0.020 m^3 polycarbonate reservoir, from which the liquid was fed to the inlet (left side) of tubular reactor by means of a magnetic pump of 1/30 hp Little Giant, model 2MD-HC, with a flow rate capacity up to 0.00014 $m^3\ s^{-1}$. The flow rates were measured by a variable-area polycarbonate rotameter (Dwyer, model LFMB-04-A2) at the outlet of T-PECR (right side); the pipe was discharged into the Continuous Stirring Tank (CST). The liquid flow circuit was constructed from PVC tubing, 0.5-inch diameter, and the valves and connectors were made of PVC as well.

2.2 *Residence time distribution (RTD) experiments*

The experimental strategy to generate a "*step signal input*" consisted of performing a "*tracer pulse injection*" into the CST, instead of introducing the tracer injection into the reactor inlet. Instantaneously after the injection, the tracer was mixed in the bulk liquid generating a step signal; the procedure is described below.

Once the recirculation system reached the steady state (after 10 minutes of continuous operation), 20.0 mL of eriochrome black T solution, as a tracer, at a concentration of 988.32 ppm (D_M = 3.23×10^{-10} $m^2\ s^{-1}$ (Armstrong *et al.*, 1988) were injected into the CST, equipped with a stirring system (a variable speed agitator and axis with three propellers). The instantaneous injection of the tracer into the recirculation tank was completely homogenized in less than 2 seconds at 800 rpm, giving a step signal. Immediately after the tracer injection, the valve V2 was closed, and the valve V3 was opened, preventing the tracer recirculation in the CST. The tracer concentration at the reactor outlet was determined with a Thermo Scientific Genesys 10S UV-vis spectrophotometer equipped with a flow cell. The bypass of the liquid sample from the outlet distributor to the flow cell (1cm of the light beam) was connected through a flexible 10-cm hose (I.D 24mm); the software of the equipment recorded data at 5-second intervals.

The discrete data of the tracer concentration as a function of time used to validate the theoretical simulation results were smoothed by means of averaging a set of point measurement data (Eq. (1)).

$$c_{i_{av}} = \frac{c_i \cdots + \ldots c_n}{n} \tag{1}$$

A set of RTD experiments in the tubular reactor was carried out using the step signal input. The volumetric flows (Q) employed were 0.37, 0.5, 0.75, 1.0, 2.0, 3.0, 4.0 L min^{-1}, corresponding to the superficial velocities u_{sup} = 0.0125, 0.0164, 0.0249, 0.0329, 0.0658, 0.0987 and 0.1316 m s^{-1}, respectively. Finally, $u_{sup} = Q/A_t$, where A_t is the cross section area of the reactor inlet.

3 Theoretical analysis

3.1 *Hydrodynamic Model*

To describe the hydrodynamics within the T-PECR in turbulent regime, the model of Reynolds Averaged Navier-Stokes for low-Reynolds close to walls (RANS-LR) (Eq. 2) in steady state coupled with the continuity equation for incompressible fluid (Eq. 3)

were solved

$$\rho\mathbf{U}\cdot\nabla\mathbf{U}+\nabla\cdot(\rho\mathbf{u}'\otimes\mathbf{u}')=-\nabla P+\nabla\cdot\mu_T(\nabla\mathbf{U}+\mathbf{U}^T)+\mathbf{F} \quad (2)$$

$$\rho\nabla\cdot\mathbf{U}=0 \quad (3)$$

where $\mathbf{U}$ is the average velocity field, μ_T is the eddy viscosity, also known as the turbulent viscosity, and $\nabla\cdot(\rho\mathbf{u}'\otimes\mathbf{u}')$ is the outer vector product, which represents interaction between the fluctuating velocities and is referred to as the Reynolds stress tensor. The expression used to determine the turbulent viscosity μ_T is:

$$\mu_T=\rho C_\mu\frac{k^2}{\varepsilon} \quad (4)$$

where $C_\mu = 0.09$ is a model constant, k is the turbulent kinetic energy and ε is the dissipation rate of turbulence energy. The constants k and ε are dependent variables involved in two additional transport equations in the RANS-LR model. It is important to note that, unlike to standard $k-\varepsilon$ model, the RANS-LR model introduces damping functions to describe the velocity field close to walls [33]. The complete model equations can be consulted in (Abe *et al*., 1994; Wilcox, 1998).

The boundary conditions employed to solve the RANS-LR were:

(a) At the inlet (constant velocity entry):

$$\mathbf{U}=U_0\cdot n,\ \kappa=\frac{3}{2}(U_0L_T)^2,\ \varepsilon=C_\mu^{3/4}\frac{\kappa^{3/2}}{L_T} \quad (5)$$

where U_0 is the initial average velocity at the inlet of the reactor, which was calculated taken into account the transversal area of the tube that fed the liquid flow.

b) At the walls (no slip condition):

Since the velocity diminishes to zero on the walls of the reactor, the wall boundary conditions at the cells adjacent to a solid wall are:

$$\mathbf{U}=0,\ \kappa=0,\ \varepsilon=\lim_{l_w\to0}\frac{2\mu\kappa}{\rho l_W^2} \quad (6)$$

(c) At the outlet of the reactor (no gradients forces):

$$(\mu+\mu_T)(\nabla\mathbf{u}+\nabla\mathbf{u}^T)\cdot\mathbf{n}=0,\quad P=0 \quad (7)$$
$$\nabla\kappa\cdot\mathbf{n}=0$$
$$\nabla\varepsilon\cdot\mathbf{n}=0$$

Under laminar regime the term $\nabla\cdot(\rho\mathbf{u}'\otimes\mathbf{u}')$ is canceled in (Eq. 5) and it is reduced to Navier-Stokes (NS) equations (Eq. 8):

$$\rho\mathbf{U}\cdot\nabla\mathbf{U}=-\nabla P+\nabla\cdot\boldsymbol{\tau}+\mathbf{F} \quad (8)$$

Where $\mathbf{U}$ is the velocity field, $\boldsymbol{\tau}$ is the *viscous stress tensor*.

The RANS-LR model in steady state was used for turbulent flow regime and NS was used for laminar flow regime.

3.2 RTD obtained with computational fluid dynamics (CFD) using COMSOL Multiphysics

The experimental RTD curves obtained by the "step-signal input" were emulated in COMSOL Multiphysics through the mass conservation equation (convection diffusion model (9)) solved in transitory, laminar and turbulent regimes.

$$\frac{\partial c_i}{\partial t}=\nabla\cdot[(D_i+D_{I,T})\nabla c_i]-\mathbf{U}\cdot\nabla c_i \quad (9)$$
$$c_i=\tilde{c}_i+c_i'$$

where $\mathbf{U}$ is the average velocity field (determined from Eq. (2) of hydrodynamic model), c_i the average concentration field, D_i is the molecular diffusion coefficient, and $D_{i,T}$ the eddy diffusivity or turbulent diffusivity.

Eddy diffusivity can be determined by considering an analogy between transport phenomena. Assuming that eddy diffusivities for heat and mass are equal ($\alpha_T = D_{i,T}$), so dimensionless turbulence numbers Prandtl, Pr_T, and Schmidt, Sc_T, are equal too, the following Kays-Crawford model for turbulent heat transfer can be used in terms of Sc_T, (Rivero *et al*., 2012).

$$Sc_T=\left[\frac{1}{2Sc_{T\infty}}+\frac{0.3}{\sqrt{Sc_{T\infty}}}\frac{\mu_T}{\rho D_i}-\left(0.3\frac{\mu_T}{\rho D_i}\right)\left(1-\exp\left(-\frac{\rho D_i}{0.3\mu_T\sqrt{Sc_{T\infty}}}\right)\right)\right]^{-1} \quad (10)$$

where $Sc_{T\infty}=0.85$.

If the convection-diffusion model is solved in laminar regime, then $D_{i,T}$ and c_i' are zero.

$$\frac{\partial c_i}{\partial t}=\nabla\cdot(D_i\nabla c_i)-\mathbf{U}\cdot\nabla c_i \quad (11)$$

The boundary and initial conditions employed to solve Eq. (9) or (11) were:

(a) Initial condition:

$$c_i=0,\quad t\le0 \quad (12)$$

(b) At the reactor inlet (step-signal at entry):

$$c_i = c_0, \quad t > 0 \quad -\mathbf{n}\cdot\mathbf{N}_0 = U_0 c_0 \tag{13}$$

(c) At the walls (impermeable walls):

$$-\mathbf{n}\cdot\mathbf{N}_i = 0 \tag{14}$$

(d) At the reactor outlet (no gradients diffusive mass flux):

$$\underbrace{\nabla\cdot(D_i + D_{i,T})\nabla c_i = 0}_{\text{turbulent regime}} \quad \text{or} \quad \underbrace{\nabla\cdot D_i \nabla c_i = 0}_{\text{laminar regime}} \tag{15}$$

Once the tracer concentration as a function of time at the outlet reactor was obtained, the average concentration was determined through the surface integral of the cross section of the tube (outlet boundary condition), which corresponds to response curves (S-curve) of the step-signal introduced at the beginning of the T-PECR. Finally, at the reactor outlet, average concentrations of the tracer were obtained as a function of time through the surface integral of the outlet tube cross-section (outlet boundary condition). The plot obtained (c_i vs t) corresponds to the response curve ($F(t)$-curve) of the step signal introduced at the reactor inlet. The description of N-S, RANS-LR, and convection diffusion models was reported in our previous work (Cruz-Díaz et. al., 2014). The next step was to find the theoretical dimensionless $F(t)$-curve (Eq. (16)) and compare it with the experimental dimensionless curve.

$$F(t) = \frac{c_i(t)}{c_{0,s}} \tag{16}$$

where $c_{0,s}$ is the maximum concentration of the tracer at the reactor outlet in steady state.

In the case of a T-PECR with CEMs as electrodes, the solution to the hydrodynamic and mass conservation equations in the "*diamond-shaped openings*" requires a considerable computational resource. The convergence of the meshing in the simulation studies (laminar and turbulent regimes) was helped by implementing the following strategy proposed here. It consisted in dividing in half the geometry of the entire reactor, maintaining the symmetry condition, and sequentially increasing the number of boundary layer meshes near solid and electrode walls, three layers for the laminar flow and six layers for the turbulent flow (see Fig. 3).

The hydrodynamics (laminar and turbulence regimens) and mass transport (convention-diffusion equation) equations were solved in 3D using the

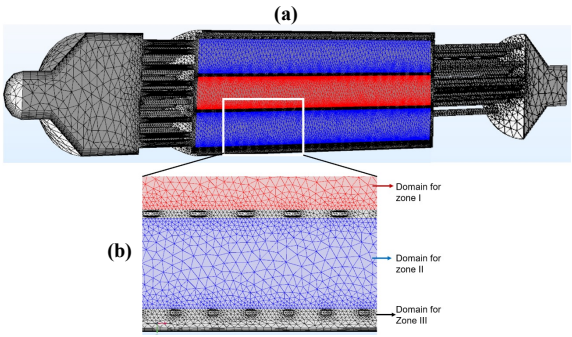

Fig. 3 (a) Meshing in COMSOL Multiphysics 5.3 for half of the entire reactor geometry (computation domain) maintaining the reactor symmetry condition. (b) Magnified view of the different zones. zone (I) delimited by the cathode mesh, zone (II) delimited by the photoanode mesh, and zone (III) delimited by the reactor wall.

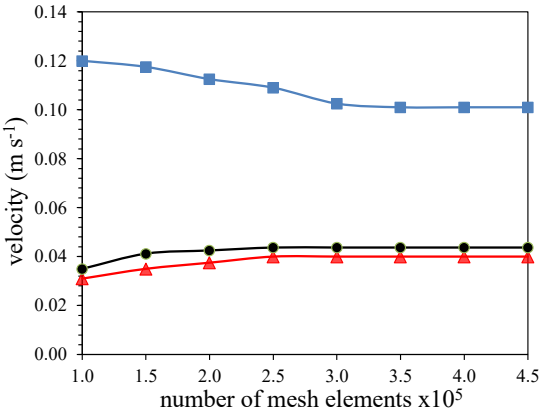

Fig. 4 Hydrodynamic simulations at different number of mesh elements for a liquid flow of 4 L m^{-1}. The velocities were taken at different distances from the reactor inlet: (■) 0.02 m, (▲) 0.10 m, and (●) 0.21 m.

software Comsol Multhiphysics 5.3, in a *Qsmio* X75-A computer equipped with a quad-core Intel® Core i7 processor, Windows® 10 Home 64-bit, 16 GB, 2.4 GHz RAM and NVIDIA® GeForce® GTX 770M 12GB video card. The computational domain meshing consisted of 354,398 cell elements, 146,078 boundary elements, 16,730 vertex elements, and 48,396 edge elements, the solver used was MUMPS.

In order to ensure that the simulation results did not depend on the mesh elements, hydrodynamic simulations at different sizes of mesh element were performed, but maintaining the liquid flow at 4 L m^{-1} to guarantee the validation of lower flows. The

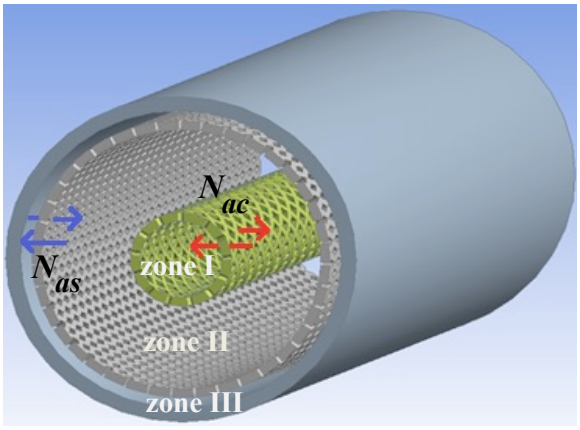

Fig. 5 View of mass exchange between zones through "diamond-shaped openings" of the meshes of anode-shell (zones II and III, grey mesh) and anode-cathode (zones I and II, green mesh).

velocities were taken at different distance from the reactor inlet (0.02, 0.10, and 0.21 m, see Fig. 4). The no dependence of the simulation results on number of mesh elements was reached using a higher element number than 3.5×10^5 elements.

Once the theoretical results obtained by using Comsol Multiphysics 5.3 were validated with the experimental $F(t)$-curves, the predictive capacity of COMSOL was used to generate the $F(t)$-curves in each zone of the T-PECR. Through these results, a global parametric model was proposed as design equations for the T-PECR.

3.3 The mathematical model proposed for the tubular reactor and its characteristic parameters

The proposed mathematical model considers that the liquid fraction inside the outer cylinder (zone II: anode) displaces at a higher velocity with respect to the liquid fraction within the inner cylinder (zone I; cathode), while the liquid fraction in the reactor shell (zone III) displaces at the lowest velocity compared to the other zones (results reported in our previous work, Jaramillo-Gutiérrez *et al*., 2020). It is also considered that there is tracer mass exchange through the "diamond-shaped openings" of the meshes, between zones I to II, and zones II to III, and vice versa (see, Fig. 5).

Fig. 6 shows a scheme of the tracer mass transport mechanisms in the three zones of the T-PECR, where the following assumptions have been considered: (a) there is no variation of the tracer mass in angular

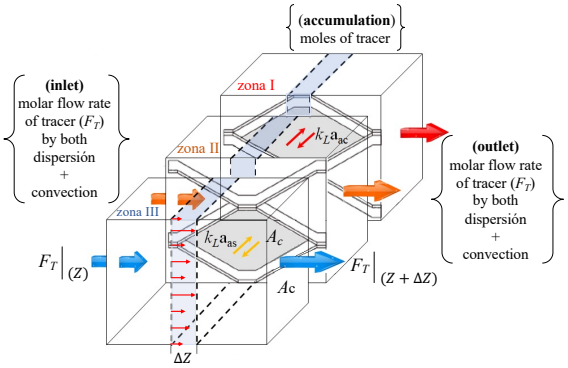

Fig. 6 Schema of the tracer mass transport mechanisms in the three zones of the T-PECR represented by differential volume elements ($A_c\Delta z$), zone I: cathode, zone II: anode, and zone III: reactor shell. In axial direction (z-axis): molar flow rate (F_T) by dispersion and convection. In lateral or radial direction: the molar flow rate towards interfaces of the diamond-shaped openings (gray color) are described by stagnant film model.

direction (θ-axis, no rotation of tracer mass about the z-axis), (b) the variation of the tracer mass in the radial direction is described with the film model, where the curvature effects of the T-PECR are neglected, under the criterion that the thickness of liquid interface in the diamond-shaped openings is much less than the diameter of the T-PECR. Therefore, (c) the main variations of the tracer mass are observed in the axial direction (z-axis).

The derivation of the governing equation the tracer mass transport in the liquid fraction (h_a) inside the outer cylinder (anode "a"), it is necessary to carry out a tracer mass balance within the differential volume element ($A_c\Delta z$) of zone II in transient regime (Eq. 17), mathematical expressions for the other zones are derived in the same way.

$$(1-h_c-h_s)(A_c\Delta z)\frac{\partial C_T^a}{\partial t} = (F_T^a\big|_z - F_T^a\big|_{z+\Delta z}) - W_{Ty}^{ac}a_{ef}(A_c\Delta y) - W_{Ty}^{as}a_{ef}(A_c\Delta y) \quad (17)$$

where the term on the left side of Eq. (17) represents the accumulation of tracer mass in the liquid fraction of zone II, h_c and h_s are the liquid fractions in the cathode and the reactor shell, respectively, the first term on the right-hand side represents the molar flow rate entering and leaving from differential volume element, according to Eq. (18). The second and third terms represent the molar flow rates towards the interfaces of the diamond-shaped openings (in radial direction) of the meshes, see below in Eqs. (21) and

(22), the parameter a_{ef} is the specific surface area, defined as the surface area per unit of reactor volume (m^2/m^3).

$$F^a_{Tz} = (A_c)W^a_{Tz} \tag{18}$$

Substituting Eq. (18) into mass conservation Eq. (17), assuming that $\Delta z = \Delta y$, dividing the expression by $(A_c \Delta z)$ and taking the limit as Δz approaches zero, we obtain the tracer molar flux balance (Eq. 19).

$$(1 - h_c - h_s)\frac{\partial C^a_T}{\partial t} = -\frac{\partial (W^a_{Tz}}{\partial z} - W^{ac}_{Ty}a_{ef} - W^{as}_{Ty}a_{ef} \tag{19}$$

where the molar flux in z-axis direction (W^a_{Tz}) considers the terms by dispersion and convection (Eq. 20), and the molar fluxes towards interfaces of the *diamond-shaped openings* (W^{ac}_{Ty} and W^{as}_{Ty}) are described by stagnant film model (Eq. 21 and 22)

$$W^a_{Tz} = -D_{ax}\frac{\partial C^a_T}{\partial Z} + u_{ef}c^a_T \tag{20}$$

$$W^{ac}_{Ty} = k^{ac}_L(c^a_T - c^c_T) \tag{21}$$

$$W^{as}_{Ty} = k^{as}_L(c^a_T - c^s_T) \tag{22}$$

Substituting Eqs. (20) to (22) into Eq. (19) yields the final equation that describe the mass transfer of tracer in zone II: anode (Eq. 23).

$$\begin{aligned}(1 - h_c - h_s)\frac{\partial C^a_T}{\partial t} =& D^a_{ax}\frac{\partial^2 C^a_T}{\partial z^2} - u^a_{ef}\frac{\partial C^a_T}{\partial z} - k_L a^{ac}_{ef}(c^a_T - c^c_T) \\ & - k_L a^{as}_{ef}(c^a_T - c^s_T)\end{aligned} \tag{23}$$

where D_{ax} is the dispersion coefficient (m^2/s), u_{ef} the effective velocity of the fluid (m/s), $k_L a_{ef}$ the volumetric mass transfer coefficient (1/s), and the superscripts (a, c and s) represents the anode, cathode and reactor shell, respectively.

The mathematical expressions that describe the tracer mass transport for cathode (zone I) and reactor shell (zone III) are the following (Eqs. (24) and (25)).

$$(1 - h_a - h_s)\frac{\partial C^c_T}{\partial t} = D^c_{ax}\frac{\partial^2 C^c_T}{\partial z^2} - u^c_{ef}\frac{\partial C^c_T}{\partial z} + k_L a^{ac}_{ef}(c^a_T - c^c_T) \tag{24}$$

$$(1 - h_a - h_c)\frac{\partial C^s_T}{\partial t} = k_L a^{as}_{ef}(c^a_T - c^s_T) \tag{25}$$

In Eq. (25) it was assume that the liquid fraction in the reactor shell behaves as a stagnant zone (lower velocity), therefore the dispersion and convection terms on the right side of Eq. (25) were neglected.

The set of equations, Eqs. (23) to (25), constitute the parametric theoretical model that describes the tracer mass balance in each zone of the T-PECR. Considering a closed-closed vessel system, the following Danckwerts-type boundary conditions and initial conditions were used (Eq. (26)).

$$\begin{aligned}
&z = 0, \quad c^a_{T0} = c^a_T(0^+) + \frac{D^a_{ax}}{u^a_{ef}}\frac{\partial c^a_T(0^+,t)}{\partial z}; \\
&z = L_z, \quad \frac{\partial c^a_T(L^-,t)}{\partial z} = 0 \\
&z = 0, \quad c^c_{T0} = c^c_T(0^+) + \frac{D^c_{ax}}{u^c_{ef}}\frac{\partial c^c_T(0^+,t)}{\partial z}; \\
&z = L_z, \quad \frac{\partial c^c_T(L^-,t)}{\partial z} = 0 \\
&t = 0, \quad c^a_T(z,t) = c^c_T(z,t) = c^s_T(t) = 0
\end{aligned} \tag{26}$$

To obtain the set of equations (equations (23) to (25)) in dimensionless form, as well as the boundary conditions and initial conditions. The following set of dimensionless variables were defined.

$$C^\beta_T = \frac{c^\beta_T}{c^\beta_{T0}},\ Z = \frac{z}{L_Z};\ u^\beta_{ef} = \frac{u^\beta_{int}}{h_\beta};\ \theta = \frac{t u^\beta_{ef}}{L}$$

$$Pe^\beta = \frac{u^\beta_{ef}L}{D^\beta_{ax}};\ N_{\beta\gamma} = \frac{k_L a^{\beta\gamma}_{ef}L_z}{u^\beta_{ef}};\ \phi_\beta = \frac{h_\beta}{h_a + h_c + h_s}$$

where β or γ represent the liquid fraction of the different zones of T-PECR, θ is dimensionless time, Pe is the Péclet number; N is the numbers of mass transfer units between anode-cathode and anode-shell, respectively; φ is the liquid hold-up ratio. Therefore, the set of equations (Eqs. (27) to (29)), constitutes the parametric theoretical model in dimensionless form.

Zone I: cathode

$$(1 - \phi_a - \phi_s)\frac{\partial C^c_T}{\partial \theta} = \frac{1}{Pe^c}\frac{\partial^2 C^c_T}{\partial Z^2} - \frac{\partial C^c_T}{\partial Z} + N_{ac}(C^a_T - C^c_T) \tag{27}$$

Zone II: anode

$$\begin{aligned}(1 - \phi_c - \phi_s)\frac{\partial C^a_T}{\partial \theta} =& \frac{1}{Pe^a}\frac{\partial^2 C^a_T}{\partial Z^2} - \frac{\partial C^a_T}{\partial Z} \\ & - N_{ac}(C^a_T - C^C_T) - N_{as}(C^a_T - C^s_T)\end{aligned} \tag{28}$$

Zone III: reactor shell

$$(1 - \phi_a - \phi_c)\frac{\partial C^s_T}{\partial \theta} = N_{as}(C^a_T - C^s_T) \tag{29}$$

The equations (27) and (29) represent the tracer mass balance in the dynamic zones (cathode and anode)

considering a plug flow with dispersion and mass exchange between zones. The Eq. (29) represents a delay zone (stagnant zone) with mass exchange between zones II and III.

The boundary conditions and initial conditions in dimensionless form (Eq. (30)) for equations (27-29):

$$Z = 0, \quad C_T^a = 1 + \frac{1}{Pe^a}\frac{\partial C_T^a(0^+,\theta)}{\partial Z}; \qquad (30)$$

$$Z = 1, \quad \frac{\partial C_T^a(1^-,\theta)}{\partial Z} = 0$$

$$Z = 0, \quad C_T^c = 1 + \frac{1}{Pe^c}\frac{\partial C_T^c(0^+,\theta)}{\partial Z};$$

$$Z = 1, \quad \frac{\partial C_T^c(1^-,\theta)}{\partial Z} = 0$$

$$\theta = 0, C_T^a(Z,\theta) = C_T^c(Z,\theta) = C_T^s(\theta) = 0$$

The numerical solution of the dimensionless mathematical model was implemented in *FlexPDE* software, 6.36s student version. The values of the N parameter were determined with the mass transfer study in COMSOL Multiphysics 5.3 by estimating the average mass transfer flux in the "diamond-shaped openings" in the meshes. The values of the φ parameter was obtained from the ratio between the volumes occupied by each zone with respect to reactor volume. The axial dispersion coefficients (D_{ax}) or the Péclet numbers (Pe) were determined by varying the D_{ax} value, and comparing the predicted response of the model with the response obtained by COMSOL until the least squares error function was minimized (S in Eq. (31))

$$S = \sqrt{\frac{\sum_i^n \left(\frac{C_{T-Comsol} - C_{Tcal}}{C_{T-Comsol}}\right)^2}{n}} \qquad (31)$$

where S is the least square error function, $C_{T-Comsol}$ is COMSOL concentration obtained by simulation (step-signal), and C_{Tcal} is the concentration calculated using Eqs. (27-29).

4 Results and discussion

4.1 COMSOL prediction of the RTD experimental curves using a step signal

The experimental RTD curves using a step signal input and the prediction obtained with COMSOL Multiphysics 5.3 for the volumetric flow rates from 0.37 to 4.0 L min^{-1} are shown in Fig. 7.

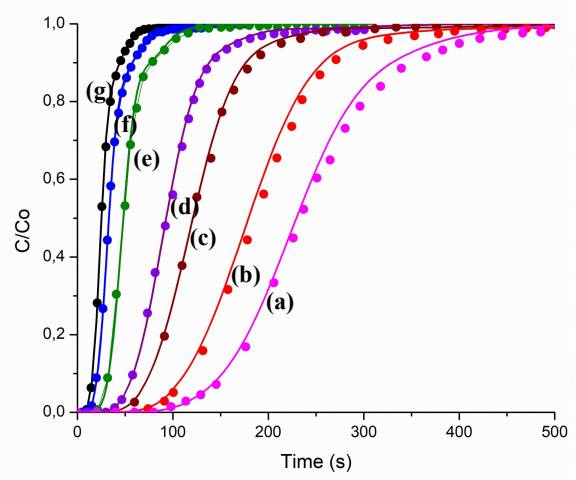

Fig. 7 Dimensionless cumulative function, $F(t)$. Experimental step signal (•) and simulation of step signal with COMSOL Multiphysics 5.3 (—). Liquid flow rates (L min-1): (a) 0.37, (b) 0.5, (c) 0.75, (d) 1.0, (e) 2.0, (f) 3.0 and (g) 4.0.

Fig. 7 shows that $F(t)$-curves obtained with COMSOL Multiphysics 5.3 agree closely with experimental data in all liquid flow rates tasted (error < 5%). Thus, the methodology implemented here is adequate to validate the CFD simulation results of the hydrodynamics and mass transport. Similar results were reported by C. Ariza *et al.*, 2018 (Ariza *et al.*, 2018). It is important to highlight that the experimental step-signal methodology employed in this work does not require a complex control system in comparison with other works (Boškovic and Loebbecke, 2008). This simple methodology is easy to implement and highly reproducible.

There are some important aspects that should be pointed out to avoid differences between the experimental data and the CFD results.

1) The system should be operating in steady state.

2) The volume of liquid in the tank should not decrease below 50%.

3) The recirculation piping should be short enough to avoid dead or delayed
times.

4) The sample point should be just in the reactor outlet.

5) An intensive mixing should be provided in the CST to avoid formation of air bubbles.

Fig. 7 also shows that as the liquid flow rate increases, the dimensionless $F(t)$-curves tend to plug flow (perfect step signal), which indicates that the presence of metallic mesh electrodes promotes the

Table 2. Summary of parameter values obtained by fitting ADM and PDE models to the RTD experimental curves.

Q (LPM)	u_{ef} (m/s)	Re	10^4 D_{ax} (m^2s^{-1})	φ	N	$(D_{ax}/u_{int}L_z)$ Global
0.37	0.00155	133	4.058	0.752	0.407	0.065
0.5	0.00188	161	3.974	0.804	0.391	0.05
0.75	0.00314	270	3.678	0.810	0.374	0.03
1	0.00419	360	3.587	0.815	0.365	0.02
2	0.00838	719	3.107	0.820	0.352	0.009
3	0.01257	1078	2.894	0.830	0.305	0.006
4	0.01676	1438	2.715	0.850	0.195	0.004

$Re^* = 2R(1-\lambda)u_{int}\rho/\mu$ where λ is the electrode diameter ratio (d_{catode}/d_{anode}).

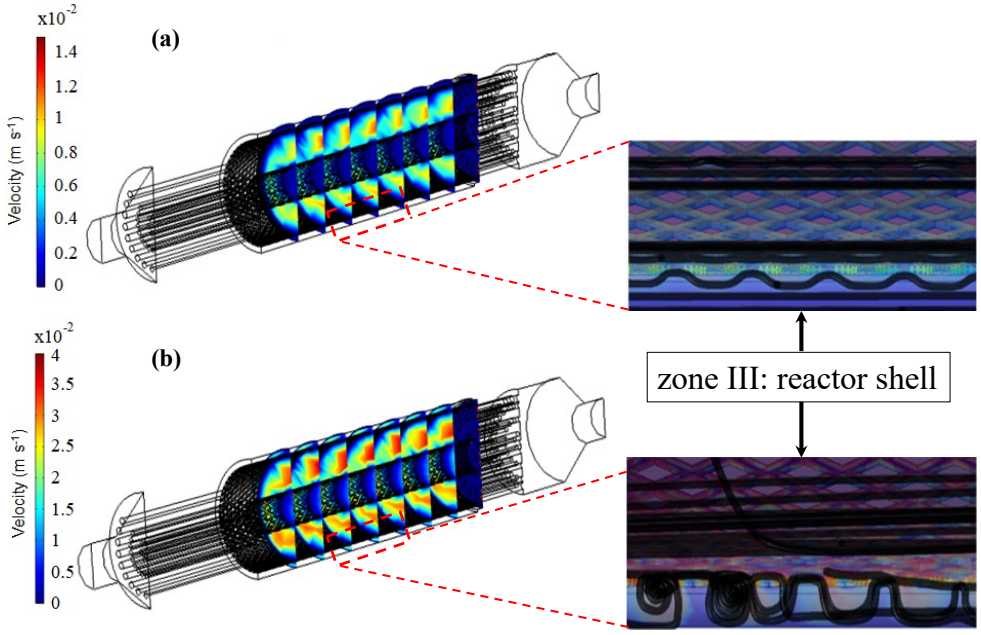

Fig. 8. 3D velocity field in slices of isosurface (left side), as well as inset of the velocity streamlines pattern (right side) for a section of zone III (reactor shell). Liquid flow rates: a) 0.37 and b) 4.0 L min^{-1}.

local turbulence. In consequence, this leads to the improvement of the convective force and the mass transfer performance, the behaviour that will be confirmed in the following sections.

Table 2 summarizes the parameter values obtained by fitting ADM and PDE models to the experimental $F(t)$ curves for all liquid flows tested.

In Table 2 it is observed that as the volumetric flow rate increases, the axial dispersion coefficient (D_{ax}) increases too, whereas the dimensionless hold-up ratio (φ) slightly increases, which indicates that the liquid flow pattern tends to ideal flow (plug flow) and that the stagnant zone decreases to some extent or begins to move at a certain velocity, respectively. On the other hand, the dimensionless number of mass transfer units (N) decreases, as the volumetric flow rate increases, indicating that at high liquid flows, the convective mass transport predominates, which facilitates the mass transport between the dynamic zone and the delay zone.

In order to evaluate the liquid flow pattern of the tubular reactor with CEMs and inlet/outlet distributors of circular sprinkler type, in the last column of Table 2 is reported the dispersion number (N_d) or the inverse Péclet number ($/Pe = D_{ax}/u_{int}L_z$). It can be observed that for all liquid flow rates tasted the N_d parameter values are in a magnitude order of small dispersion ($D_{ax}/u_{int}L_z \approx 0.01$). This confirms that the incorporation of inlet/outlet distributors in a tubular reactor improve considerably the behaviour of the liquid flow pattern.

4.2 Hydrodynamic behaviour

Fig. 8 shows the velocity field in slices of isosurface for two liquid flow rates (L min^{-1}): a) 0.37 and b) 4.0, as well as an inset of the streamlines in order to show the velocity field pattern in a section of zone III (around photoanode mesh).

In both graphics of iso-surface slices can be observed that the liquid fraction inside the outer cylinder (zone II: anode) displaces at a higher velocity with respect to the liquid fractions within the inner cylinder (zone I; cathode) and the reactor shell (zone III), confirming the proposed consideration for the mathematical model. It is also observed in the inset of velocity streamlines for photoanode mesh (zone III) that at liquid flow rate of 0.37 L min^{-1} (Fig. 8a), the streamlines do not cross the "diamond-shaped openings" of the mesh. Thus, the flow pattern inside the reactor behaves like concentric tubes with a delay zone (reactor shell); similar results were observed at 0.5, 0.75, and 1.0 L min^{-1}. However, at 4.0 L min^{-1} (Fig. 8b), the streamlines cross the "diamond-shaped openings" generating a crisscross flow in the cathode and (photo)anode meshes: This increases the interaction between the fluid elements and the walls of the meshes, resulting in the formation of micro turbulence that induces the rotation (formation of small eddies) of fluid elements (Su *et al*., 2011) and a higher intensity of mass exchanges thereby takes place in different reactor zones.

4.3 Prediction of the parametric mathematical model to the $F(t)$-curves obtained with computational simulation

Fig. 9 shows that the parametric mathematical model (solid lines) here proposed, is capable of approximating the behaviour of the $F(t)$-curves estimated with COMSOL Multiphysics 5.3 (dots) for each reactor zone.

Fig. 9 also shows that as the liquid flow increases, the dimensionless $F(t)$-curves of the zones I and II tend to join each other, and at liquid flow rates of 2.0 to 4.0 L min^{-1} the curves are practically overlapped. It confirms that at high liquid flows, the turbulence increases in the vicinity of the "diamond-shaped openings", provoking an intensive macromixing between zones I and II until the concentration in both zones becomes equal. Therefore, at higher liquid flow rates (2.0 to 4.0 L min^{-1}) the ADM is enough to describe the $F(t)$-curves in zones I and II, and the same parameter values will be used in the anodic and cathodic equations.

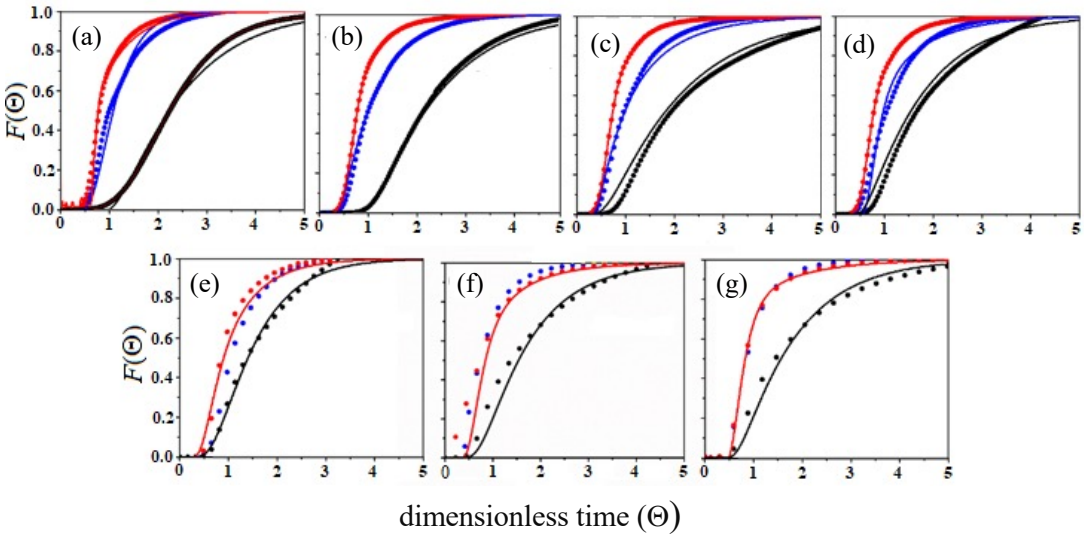

Fig. 9. Computing simulation (COMSOL Multiphysics 5.3) of the dimensionless cumulative function, $F(t)$, in each zone of the T-PECR (dots): zone I, the inner cylinder (•); zone II, the outer cylinder (•), and zone III, reactor shell (•). Predictions of the theoretical parametric model (solid lines). Liquid flow rates (L min-1): a) 0.37, (b) 0.5, (c) 0.75, (d) 1.0, (e) 2.0, (f) 3.0 and (g) 4.0.

Table 3. Parameter values used in the mathematical model to describe the $F(t)$-curves in each zone of the T-PECR.

Q (L/m)	Re^*	$10^4 u_{ef}$ (m/s)			$10^4 D_{ax}$ (m^2/s)			φ			N	
		u^a_{ef}	u^c_{ef}	u^s_{ef}	D^a_{ax}	D^c_{ax}	D^s_{ax}	φ_a	φ_c	φ_s	N_{ca}	N_{as}
0.37	133	2.99	6.22	0.339	4.02	6.134	9.014	0.098	0.632	0.27	0.549	0.727
0.5	161	20	9.31	0.623	3.971	5.89	7.965	0.095	0.696	0.209	0.498	0.639
0.75	270	28	10	0.771	2.921	5.024	7.061	0.094	0.705	0.201	0.413	0.591
1	360	61	33	1.29	2.57	4.57	5.837	0.091	0.712	0.197	0.375	0.431
2	719	120	81	3.04	3.005	3.005	4.227	0.089	0.7	0.201	0	0.425
3	1078	171	145	3.86	2.801	2.801	3.512	0.088	0.705	0.21	0	0.302
4	1438	230	6.64	6.64	2.705	2.705	3.094	0.087	0.71	0.193	0	0.195

The subscripts N_{ac} and N_{as} represent the mass transfer units between anode-cathode and anode-shell zones, respectively.

Table 4. Dispersion numbers for each reactor zone.

Q (L/m)	Re	N^a_d	N^c_d	N^s_d
0.37	133	0.336	0.247	6.647
0.5	161	0.05	0.158	3.196
0.75	270	0.026	0.126	2.29
1	360	0.011	0.035	1.131
2	719	0.006	0.009	0.348
3	1078	0.004	0.005	0.227
4	1438	0.003	0.003	0.116

On the other hand, the $F(t)$-curves of the zone III are markedly extended with respect to the other two zones, confirming that the annular space between the (photo)anode and the reactor shell can be modelled mathematically as delay zone with mass exchange with zone II (Eq. 29). Table 3 reports the parameter values used in the parametric mathematical model.

Table 3 shows that the effective velocities in the reactor shell zone are lower than those obtained in the anode and cathode zones, confirming that the fluid elements in the reactor shell are markedly delayed or stagnant. On the other hand, as the liquid flow rate increases, the D_{ax} values decrease (increase in the Pe numbers), indicating that the flow pattern tends to plug flow (a perfect step signal). It is also observed that when the liquid flow rate increases, the φ parameter decreases slightly for zones I and III, but increases for the zone II, which indicates that delay zones (I and III) tend to move at high flow rates. This behaviour was confirmed in Fig. 8(b), where at 4.0 L min^{-1}, the crisscross flow was observed to promote the formation of eddies in zones I and III. However, the N parameter decreases as the liquid flow rate increases, indicating that at high liquid flow the convective mass transport predominates, facilitating the mass transport between the zones (from I to II, and from II to III, and vice versa), while at low liquid flows, diffusional transport predominates, making the mass transport slower. Therefore, a large number of mass transfer units (N) indicate a slow mass transfer rate. On the other hand, because for the liquid flows of 2.0, 3.0, and 4.0 L min^{-1} the $F(t)$-curves are practically overlapped, the N values for these flows are zero.

Table 4 shows the computing of the dispersion number (N_d) for each liquid flow or Reynolds number (Re).

In Table 4 it is observed that the N_d decrease as the liquid flow increases and each zone has different values. For the zone II (photoanode) and zone I (cathode) in the ranges of ($161 \leq \mathrm{Re} \leq 1438$) and ($360 \leq \mathrm{Re} \leq 1438$), respectively; the N_d values have an order of magnitude of low dispersion. For the zone III (reactor shell), in all liquid flows, the N_d values have an order of magnitude of high dispersion, and for the interval of ($133 \leq \mathrm{Re} \leq 360$) the $N_d \geq 1.0$, confirming that it is not valid to apply the ADM for these liquid flows, which means that the liquid flow pattern in zone III tends to behave as a mixing tank (Levenspiel, 1999). For this reason, there was no good fit between the $F(t)$-curves of CFD and the PDE mathematical model (results not shown).

Conclusions

In the present work, the liquid flow pattern of a tubular reactor with concentric expanded meshes (CEMs) and inlet/outlet distributors of circular sprinkler type was evaluated. A novelty experimental methodology of step signal input was implemented to validate the RTD theoretical curves (cumulative function, $F(t)$-curves) obtained with CFD. Subsequently, CFD was used for generating the $F(t)$-curves in the different zones of the tubular reactor, which were approximated with the PDE model to obtain the design equations of the

tubular reactor.

It was observed that the global $F(t)$-curves (macromixing scale) obtained with COMSOL Multiphysics 5.3 agree closely with experimental data in all liquid flow rates tasted. Thus, the experimental step-signal methodology employed in this work is adequate to validate the computational simulation results of the hydrodynamics and mass transport. Furthermore, this simple methodology is easy to implement and highly reproducible.

It was observed that for all liquid flow rates tasted, the N_d parameter values are in a magnitude order of small dispersion ($D_{ax}/u_{int}L_z \approx 0.01$). This confirms that the incorporation of inlet/outlet distributors in a tubular reactor improve considerably the behaviour of the liquid flow pattern.

The set of design equations of the parametric mathematical model here proposed is capable of approximating adequately the behaviour of the $F(t)$-curves generated with CFD in each reactor zone. It is also observed that as the liquid flow increases, the dimensionless $F(t)$-curves in the anodic and cathodic zones tend to join each other, and at liquid flow rates from 2.0 to 4.0 L min^{-1} the curves are practically overlapped. Therefore, at higher liquid flow rates, the same parameter values will be used in the anodic and cathodic equations. However, in the reactor shell zone micro turbulence were observed that induces the rotation (formation of small eddies) of fluid elements, confirming that in the annular space between the (photo)anode and the reactor shell, an equation of mixing tank agree closely with CFD data in all liquid flow rates tasted.

Therefore, this experimental methodology coupled with the theoretical analysis of micro/macromixing of RTD curves with CFD can be a good alternative to establish the reactor design equations.

Acknowledgments

This work has been carried out with the financial support of COLCIENCIAS through the project 110265843664 (VIE code 8836) and Instituto Colombiano del Petróleo - ICP, ECOPETROL through the academic agreement No. 5222395 (Convenio Marco de Cooperación Tecnológica y Científica UIS-ECOPETROL S.A.). The authors thank Laboratorio Multidiciplinario (LEM)-FES Cuautitlán of the Universidad Nacional Autónoma de México. M.I. Jaramillo-Gutierrez also gives thanks to COLCIENCIAS for the studentship within the PhD program “Doctorados Nacionales No.647-2014".

References

Abe, K., Kondoh, T., Nagano, Y. (1994). A new turbulence model for predicting fluid flow and heat transfer in separating and reattaching flows-I. Flow field calculations. *International Journal of Heat and Mass Transfer 37*, 139-151, https://doi.org/10.1016/0017-9310(94)90168-6

Ariza, C., Casado, C., Wang, R. Q., Adams, E., Marugán, J. (2018). Comparative evaluation of OpenFOAM® and ANSYS® Fluent for the modeling of annular reactors. *Chemical Engineering Technology 41(7)*, 1473-1483. https://doi.org/10.1002/ceat.201700455

Armstrong, D., Menges, R., Han, S. (1988). Evaluation of dye-micelle binding constants using diffusion sensitive band broadening effects. *Journal of Colloid and Interface Science 126*, 239-242. https://doi.org/10.1016/0021-9797(88)90117-8

Barbosa de Matos, D., Barbosa, M. P. R., Monteiro L. O., Ribeiro, S. J., Silva, L. N., Hortense T. N., Nogueira, M. M., Sánchez de Alsina, O. L., Bezerra C. E. (2020). Characterization of a tubular electrochemical reactor for the degradation of the commercial diuron herbicide. *Environmental Technology 41(10)*, 1307-1321. https://doi.org/10.1080/09593330.2018.1531941

Boškovic, D. and Loebbecke, S. (2008). Modelling of the residence time distribution in micromixers. *Chemical Enginering Journal 135*, 138-146. https://doi.org/10.1016/j.cej.2007.07.058

Cardoso, J.C., Bessegato, G.G., Boldrin Zanoni, M.V. (2016). Efficiency comparison of ozonation, photolysis, photocatalysis and photoelectrocatalysis methods in real textile wastewater decolorization. *Water Research 98*, 39-46. https://doi.org/10.1016/j.watres.2016.04.004

Casado, C., Marugán, J., Timmers, R., Muñoz, M., van Grieken, R. (2017). Comprehensive multiphysics modeling of photocatalytic processes by computational fluid dynamics

based on intrinsic kinetic parameters determined in a differential photoreactor. *Chemical Engineering Journal 310*, 368-380. https://doi.org/10.1016/j.cej.2016.07.081

Christensen, P.A., Curtis, T.P., Egerton, T.A., Kosa, S.A.M., Tinlin, J.R. (2003). Photoelectrocatalytic and photocatalytic disinfection of *E. coli* suspensions by titanium dioxide. *Applied Catalysis B: Environmental 41(4)*, 371-386. https://doi.org/10.1016/S0926-3373(02)00172-8

Christensen, P.A., Egerton, T.A., Kosa, S.A.M., Tinlin, J.R., Scott, K. (2005). The photoelectrocatalytic oxidation of aqueous nitrophenol using a novel reactor. *Journal of Applied Electrochemistry 35(7-8)*, 683-692. https://doi.org/10.1007/s10800-005-1366-8

Cruz-Díaz, M.R., Rivero, E.P., Almazán-Ruiz, F.J., Torres-Mendoza, Á., González, I. (2014). Design of a new FM01-LC reactor in parallel plate configuration using numerical simulation and experimental validation with residence time distribution (RTD). *Chemical Engineering Process: Process Intensification 85*, 145-154. https://doi.org/10.1016/j.cep.2014.07.010

Divyapriya, G., Singh, S., Martínez-Huitle, C. A., Scaria, J., Karim, A. V., Nidheesh, P. V. (2021). Treatment of real wastewater by photoelectrochemical methods: An overview. *Chemosphere 276*, 130188. https://doi.org/10.1016/j.chemosphere.2021.130188

Djoudi, W., Aissani-Benissada, F., Ozilb, P. (2012). Flow modeling in electrochemical tubular reactor containing volumetric electrode: Application to copper cementation reaction. *Chemical Engineering Research and Design 90(10)*, 1582-1589. https://doi.org/10.1016/j.cherd.2012.02.003

Fitch, A.W. and Ni, X., (2003). On the determination of axial dispersion coefficient in a batch oscillatory baffled column using laser induced fluorescence. *Chemical Engineering Journal 92*, 243-253. https://doi.org/10.1016/S1385-8947(02)00261-9

Ibrahim, D.S., Veerabahu, C., Palani, R., Devi, S., Balasubramanian, N. (2013). Flow dynamics and mass transfer studies in a tubular electrochemical reactor with a mesh electrode. *Computer & Fluids 73*, 97-103. https://doi.org/10.1016/j.compfluid.2012.12.001

Jaramillo-Gutiérrez, M.I., Carreño-Lizcano, M.I., Ruiz-Lizarazo, J.O., Pedraza-Avella, J.A., Rivero, E.P., Cruz-Díaz, M.R. (2020). Design, mathematical modelling, and numerical simulation of a novel tubular photoelectrochemical reactor and experimental validation by residence time distribution and mass transfer coefficients. *Chemical Engineering Journal 386*, 123895. https://doi.org/10.1016/j.cej.2019.123895

Jaramillo-Gutiérrez, M.I., Rivero, E.P., Cruz-Díaz, M.R., Niño-Gómez, M.E., Pedraza-Avella, J.A. (2016). Photoelectrocatalytic hydrogen production from oilfield-produced wastewater in a filter-press reactor using TiO_2-based photoanodes. *Catalysis Today 266*, 17-26. https://doi.org/10.1016/j.cattod.2015.12.008

Levenspiel, O. (1999). *Chemical Reaction Engineering*, 3rd ed. Industrial & Engineering Chemistry Research. John Wiley, New York. https://doi.org/10.1021/ie990488g

Martínez-Delgadillo, S.A., Mollinedo P., H.R., Gutiérrez, M.A., Barceló, I.D., Méndez, J.M. (2010). Performance of a tubular electrochemical reactor, operated with different inlets, to remove Cr(VI) from wastewater. *Computer & Chemical Engineering 34(4)*, 491-499. https://doi.org/10.1016/j.compchemeng.2009.05.016

Marugán, J., van Grieken, R., Pablos, C., Adán C., Timmers R. (2013). Determination of photochemical, electrochemical and photoelectrochemical efficiencies in a photoelectrocatalytic reactor. *International Journal of Chemical Reactor Engineering 11(2)*, 787-797. https://doi.org/10.1515/ijcre-2012-0014

McMichaela, S., Wasob, M., Reynekeb, B., Khanb, W., Byrnea, J. A., Fernandez-Ibanez, P. (2021). Electrochemically assisted photocatalysis for the disinfection of rainwater under solar

irradiation. *Applied Catalysis B: Environmental 281*, 119485. https://doi.org/10.1016/j.apcatb.2020.119485

Moraes, P. B., Pelegrino R.R.L., Bertazzoli R. (2007). Degradation of Acid Blue 40 dye solution and dye house wastewater from textile industry by photoassisted electrochemical process. *Journal of Environmental Science and Health Part A 42(14)*, 2131-2138. https://doi.org/10.1080/10934520701629591

Pablos, C., Marugán, J., van Grieken, R., Adán, C., Riquelme, A., Palma, J. (2014). Correlation between photoelectrochemical behaviour and photoelectrocatalytic activity and scaling-up of P25-TiO_2 electrodes. *Electrochimica Acta 130*, 261-270. https://doi.org/10.1016/j.electacta.2014.03.038

Rivero, E.P., Rivera, F.F., Cruz-Díaz, M.R., Mayen, E., González, I. (2012). Numerical simulation of mass transport in a filter press type electrochemical reactor FM01-LC: comparison of predicted and experimental mass transfer coefficient. *Chemical Engineering Research and Design 90 (11)*, 1969-1978. https://doi.org/10.1016/j.cherd.2012.04.010

Roy, S. (2017). Radiotracer and particle tracking methods, modeling and scale-up. *American Institute of Chemical Engineers AIChE Journal 63*, 314-326. https://doi.org/10.1002/aic.15559

Su, J., Lu, H.-Y., Xu, H., Sun, J.-R., Han, J.-L., Lin, H.-B. (2011). Mass transfer enhancement for mesh electrode in a tubular electrochemical reactor using experimental and numerical simulation method. *Russian Journal of Electrochemistry 47*, 1293-1298. https://doi.org/10.1134/S1023193511110140

Suhadolnik, L., Pohar, A., Novak, U., Likozar, B., Mihelič, A., Čeh, M. (2019). Continuous photocatalytic, electrocatalytic and photo-electrocatalytic degradation of a reactive textile dye for wastewater-treatment processes: Batch, microreactor and scaled-up operation. *Journal of Industrial and Engineering Chemistry 72*, 178-188. https://doi.org/10.1016/j.jiec.2018.12.017

Takeda, Y. (1999). Ultrasonic Doppler method for velocity profile measurement in fluid dynamics and fluid engineering. *Experiments in Fluids 46(3)*, 177-178. https://doi.org/10.1007/s003480050277

Turolla, A., Fumagalli, M., Bestetti M. Antonelli, M. (2012). Electrophotocatalytic decolorization of an azo dye on TiO_2 self-organized nanotubes in a laboratory scale reactor. *Desalination 285*, 377-382. https://doi.org/10.1016/j.desal.2011.10.029

Turolla, A., Bestetti, M., Antonelli, M. (2018). Optimization of heterogeneous photoelectrocatalysis on nanotubular TiO_2 electrodes: Reactor configuration and kinetic modelling. *Chemical Engineerin Science 182*, 171-179. https://doi.org/10.1016/j.ces.2018.02.041

Upadhyay, R.K., Pant, H.J., Roy, S. (2013). Liquid flow patterns in rectangular air-water bubble column investigated with Radioactive Particle Tracking. *Chemical Engineering Science 96*, 152-164. https://doi.org/10.1016/J.CES.2013.03.045

Wang, J., Li, T., Zhou, M., Li, X., Yu, J. (2015). Characterization of hydrodynamics and mass transfer in two types of tubular electrochemical reactors. *Electrochimica Acta 173*, 698-704. https://doi.org/10.1016/j.electacta.2015.05.135

Wilcox, D.C. (1998). *Turbulence Modeling for CFD*, third ed., DCW Industries, California.

Zhao, X., Qu, J., Liu, H., Wang, C., Xiao S., Liu, R., Liu, P., Lan, H., Hu, C. (2010). Photoelectrochemical treatment of landfill leachate in a continuous flow reactor. *Bioresource Technology 101(3)*, 865-869. https://doi.org/10.1016/j.biortech.2009.08.098

Zhao, X., Guo, L., Qu, J. (2014). Photoelectrocatalytic oxidation of Cu-EDTA complex and electrodeposition recovery of Cu in a continuous tubular photoelectrochemical reactor. *Chemical Engineering Journal 239*, 53-59. https://doi.org/10.1016/j.cej.2013.10.088